

# Cohesin mutations alter DNA damage repair and chromatin structure and create therapeutic vulnerabilities in MDS/AML

Zuzana Tothova,<sup>1,2</sup> Anne-Laure Valton,<sup>3</sup> Rebecca A. Gorelov,<sup>2</sup> Mounica Vallurupalli,<sup>1,2</sup> John M. Krill-Burger,<sup>2</sup> Amie Holmes,<sup>4</sup> Catherine C. Landers,<sup>2</sup> J. Erika Haydu,<sup>2</sup> Edyta Malolepsza,<sup>2</sup> Christina Hartigan,<sup>2</sup> Melanie Donahue,<sup>2</sup> Katerina D. Popova,<sup>2</sup> Sebastian Koochaki,<sup>1</sup> Sergey V. Venev,<sup>3</sup> Jeanne Rivera,<sup>5</sup> Edwin Chen,<sup>5</sup> Kasper Lage,<sup>2</sup> Monica Schenone,<sup>2</sup> Alan D. D'Andrea,<sup>4</sup> Steven A. Carr,<sup>2</sup> Elizabeth A. Morgan,<sup>6</sup> Job Dekker,<sup>3,7</sup> and Benjamin L. Ebert<sup>1,2,7</sup>

<sup>1</sup>Department of Medical Oncology, Dana-Farber Cancer Institute, Boston, Massachusetts, USA. <sup>2</sup>Cancer Program, Broad Institute, Cambridge, Massachusetts, USA. <sup>3</sup>Program in Systems Biology, Department of Biochemistry and Molecular Pharmacology, University of Massachusetts Medical School, Worcester, Massachusetts, USA. <sup>4</sup>Department of Radiation Oncology, Dana-Farber Cancer Institute, Boston, Massachusetts, USA. <sup>5</sup>Faculty of Biological Sciences, University of Leeds, Leeds, United Kingdom. <sup>6</sup>Department of Pathology, Brigham and Women's Hospital, Boston, Massachusetts, USA. <sup>7</sup>Howard Hughes Medical Institute, Chevy Chase, Maryland, USA.

The cohesin complex plays an essential role in chromosome maintenance and transcriptional regulation. Recurrent somatic mutations in the cohesin complex are frequent genetic drivers in cancer, including myelodysplastic syndromes (MDS) and acute myeloid leukemia (AML). Here, using genetic dependency screens of stromal antigen 2-mutant (*STAG2*-mutant) AML, we identified DNA damage repair and replication as genetic dependencies in cohesin-mutant cells. We demonstrated increased levels of DNA damage and sensitivity of cohesin-mutant cells to poly(ADP-ribose) polymerase (PARP) inhibition. We developed a mouse model of MDS in which *Stag2* mutations arose as clonal secondary lesions in the background of clonal hematopoiesis driven by tet methylcytosine dioxygenase 2 (*Tet2*) mutations and demonstrated selective depletion of cohesin-mutant cells with PARP inhibition in vivo. Finally, we demonstrated a shift from *STAG2*- to *STAG1*-containing cohesin complexes in cohesin-mutant cells, which was associated with longer DNA loop extrusion, more intermixing of chromatin compartments, and increased interaction with PARP and replication protein A complex. Our findings inform the biology and therapeutic opportunities for cohesin-mutant malignancies.

**Authorship note:** BLE and ZT are co-corresponding authors.

**Conflict of interest:** ADD consults for Eli Lilly and Company, EMD Serono, Sierra, and Cedilla Therapeutics; SAC is on the scientific advisory board for Kymera Therapeutics, Seer, and PTM Biolabs and is a consultant for Biogen and Pfizer; and BLE has received research support from Celgene and Deerfield and consulting fees from Grail.

**Copyright:** © 2021, Tothova et al. This is an open access article published under the terms of the Creative Commons Attribution 4.0 International License.

**Submitted:** July 15, 2020

**Accepted:** December 16, 2020

**Published:** February 8, 2021

**Reference information:** *JCI Insight*. 2021;6(3):e142149.  
<https://doi.org/10.1172/jci.insight.142149>.

## Introduction

The cohesin complex is a multimeric protein complex that forms a ring structure around DNA molecules and plays multiple key roles in spatial organization of eukaryotic genomes. Cohesin proteins are involved in several essential cellular functions, including sister chromatid cohesion, chromatin loop organization, transcriptional activation, and DNA replication and damage repair, among others (reviewed in ref. 1). More recently, the cohesin complex was identified as one of the most frequently mutated protein complexes in cancer, including myeloid malignancies, glioblastoma, breast cancer, bladder cancer, and Ewing sarcoma (2, 3). The mechanisms by which cohesin mutations cause cellular transformation are unknown, and currently no therapies are known to exhibit selective efficacy in cohesin-mutant cancers.

Myelodysplastic syndromes (MDS) and acute myeloid leukemia (AML) are clonal diseases of mutated hematopoietic stem and progenitor cells (HSPCs) characterized by abnormal differentiation and proliferation caused by somatic mutations in genes encoding transcription factors, epigenetic regulators, chromatin modifiers, and splicing factors (4, 5). The core components of the cohesin complex, stromal antigen 2 (*STAG2*), structural maintenance of chromosomes 1 (*SMC1*), *SMC3*, and *RAD21*, as well as its modulators, *PDS5* and *NIPBL* cohesin loading factor (*NIPBL*), are collectively mutated in 13% of patients with de novo AML, 21% of patients with secondary AML, and 11% of patients with MDS, where they are associated with poor overall survival (5–10). Mutations in the cohesin genes are nearly always mutually exclusive, heterozygous,

predicted loss-of-function (LOF) lesions, which are thought to be acquired early during the progression from clonal hematopoiesis of indeterminate prognosis to MDS (4, 11). Targeted inactivation of *Smc3* or *Stag2*, and overexpression of mutant cohesin genes in WT mouse and human HSPCs, have been previously studied (12–15), but no cohesin-mutant models currently exist that recapitulate the natural evolution of cohesin-mutant myeloid disease in the context of clonal hematopoiesis.

Two cohesin complexes are known to co-occur in somatic vertebrate cells, each containing the core components SMC1A, SMC3, and RAD21, and alternatively including STAG2 or the less abundant STAG1 (16). STAG2- and STAG1-containing complexes associate with centromeres and telomeres, respectively, but their sister chromatid cohesion-independent functional differences are not fully understood (1). *STAG2* mutations account for over 85% of cohesin mutations in MDS, whereas *STAG1* is rarely mutated in MDS or AML (6, 7, 10, 17). The mechanism underlying clonal expansion of these driver mutations is unlikely related to defects in sister chromatid cohesion given lack of association between *STAG2* mutations and complex karyotype and aneuploidy (10, 18). STAG1- versus STAG2-containing complexes have been recently shown to differentially contribute to chromatin organization, facilitating longer loops at topologically associating domain (TAD) boundaries and shorter, more transient nested enhancer-promoter contacts, respectively (19–22). Furthermore, deficiency of *Stag2* and RUNX family transcription factor 1 (*Runx1*) has been shown to disrupt enhancer-promoter looping and affect transcriptional pausing leading to selective gene dysregulation (22).

We sought to determine the effects of *STAG2* mutations observed in patients on the cohesin complex composition and genetic dependencies, with the goal of understanding the mechanisms by which these mutations contribute to cellular transformation and how cohesin-mutant malignancies could be therapeutically targeted.

## Results

*Genetic synthetic vulnerabilities in STAG2-mutant cells.* To study the cellular consequences of cohesin mutations in myeloid malignancies, we used CRISPR/Cas9 to engineer a spectrum of predicted LOF *STAG2*, *SMC3*, and *RAD21* mutations identified in patients in AML cell lines WT for all cohesin subunits and modulators. The different mutants largely phenocopy one another and are consistent with loss of function of *STAG2* or haploinsufficiency of *SMC3* or *RAD21* (Supplemental Figure 1, A–G; supplemental material available online with this article; <https://doi.org/10.1172/jci.insight.142149DS1>; see Methods). We first focused on *STAG2*, the most frequently mutated subunit of the cohesin complex, and hypothesized that different *STAG2* mutations would be associated with mutant-specific genetic dependencies.

We performed genome-scale CRISPR/Cas9 screens in 6 WT and 5 *STAG2*-mutant U937 cell lines representing different *STAG2* mutations using the Avana sgRNA library, which targets a total of 20,000 protein-coding genes with 4 unique sgRNAs per gene and includes 1000 nontargeting sgRNA controls (23). We observed that *STAG2*-mutant cells were strongly dependent on *STAG1*, as has been recently reported in the context of bladder cancer and Ewing sarcoma cell lines (24, 25) (Figure 1A and Supplemental Figure 2A). Since both STAG1- and STAG2-containing cohesin complexes participate in sister chromatid cohesion, we examined whether loss of *STAG1* in *STAG2*-deficient cells would lead to aberrant sister chromatid cohesion. We found that loss of both *STAG1* and *STAG2*, but not loss of either one alone, led to sister chromatid cohesion defects as assessed by premature centromere separation and railroad chromosomes (Figure 1B), providing a mechanistic basis for the synthetic lethality of *STAG1* and *STAG2*. The absence of sister chromatid cohesion defects in cells harboring loss of *STAG2* alone is in agreement with lack of aneuploidy or complex karyotype in patients with *STAG2*-mutant MDS and AML (5, 10, 26), as well as previous studies in yeast suggesting that sister chromatid cohesion is unaffected with up to 87% loss of cohesin levels (27). Therefore, *STAG2*-mutant cells are dependent on the presence of *STAG1* and do not have overt sister chromatid cohesion defects unless accompanied by a simultaneous loss of *STAG1*.

In addition to *STAG1*, we identified preferential dependency of *STAG2*-mutant cells on multiple components of the DNA damage repair and replication machinery (Figure 1A), as well as lineage-defining transcription factors, and genes involved in mRNA processing (Supplemental Table 1). Of note, we identified multiple members of the base excision repair [poly(ADP-ribose) polymerase 1; PARP1], homologous recombination (BRIP1, RAD51B, RAD51C, RAD54L2, XRCC2, XRCC3, PARP1), mismatch repair (MSH2; DNA polymerase delta 3, accessory subunit [POLD3]; EXO1), and DNA replication (replication protein A2 [RPA2], POLD3) machineries as specific synthetic vulnerabilities of *STAG2*-mutant cells (Figure 1A). Therefore, we observed differential dependency of *STAG2*-mutant cells on DNA damage repair and replication-associated pathways.

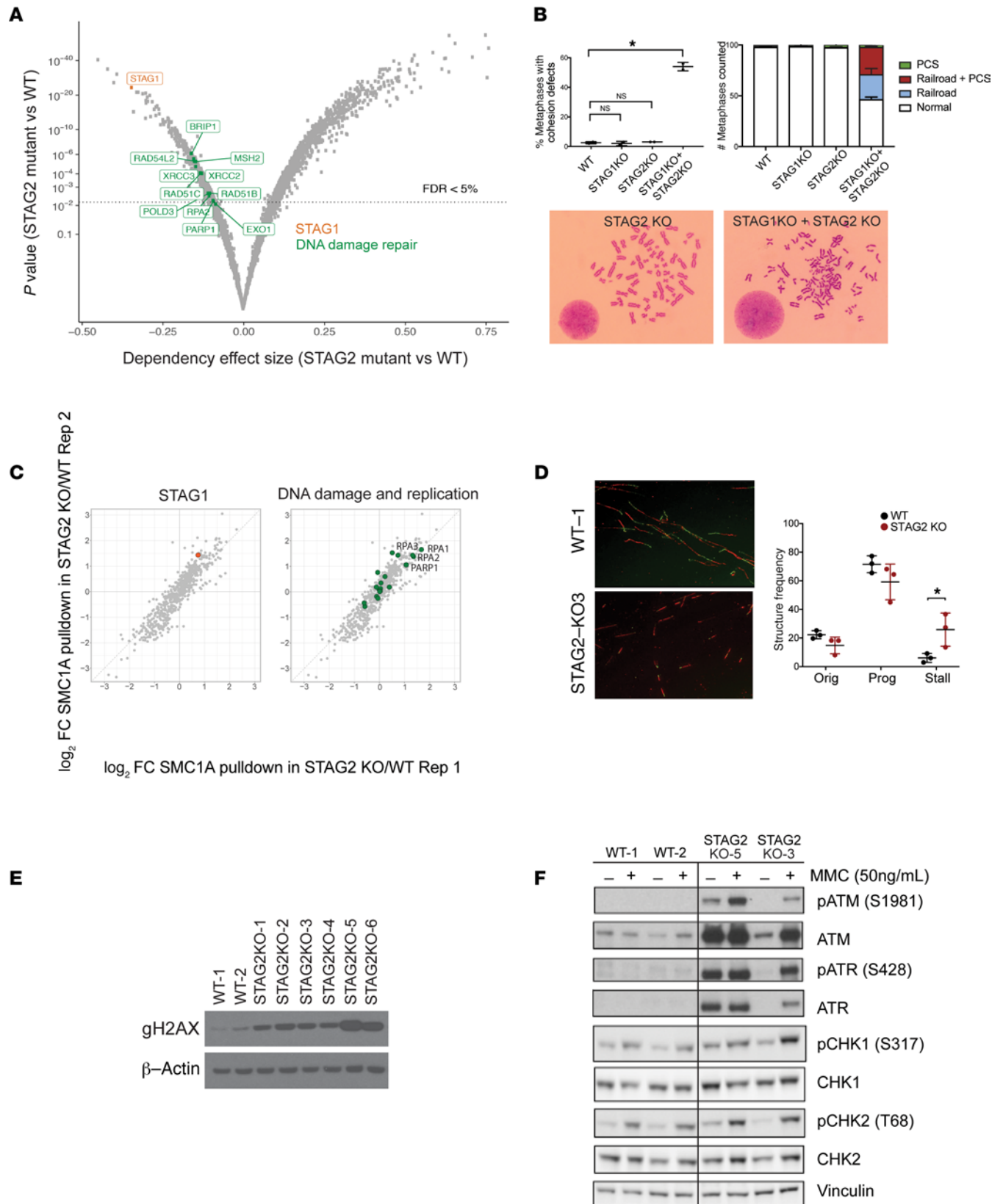


**Figure 1. Identification of DNA replication and damage repair as a dependency in *STAG2*-mutant cells.** (A) Volcano plot depicting differential dependencies in *STAG2*-mutant versus WT cells. Composite data for 5 *STAG2*-mutant cell lines (U937 *STAG2*-KO2, *STAG2*-KO3, KOC5, KOD5C, KOG8B) and 6 *STAG2*-WT cell lines (U937 WT-1, WT-2, NCB1, NCB12, NCB2A, NCC4) are shown. Respective sets of genes representing dependency in *STAG2*-mutant over WT cells with FDR < 5% are shown in color. (B) Cohesion defect analysis in WT, *STAG1*-, *STAG2*-, and double *STAG1/STAG2*-knockout cells. Mean  $\pm$  SD is shown for 2 independent biological replicates of *STAG2*-WT (U937 WT-1, WT-2) and *STAG2*-knockout cells (U937 *STAG2*-KO3, *STAG2*-KO4) transduced with *STAG1* or control sgRNAs. For

each sample 100 metaphase spreads were scored. \* $P < 0.0001$  (1-way ANOVA). PCS, premature centromere separation; Railroad, railroad chromosomes. (C) Log<sub>2</sub> fold change (FC) of protein enrichment after SMC1A IP-MS in WT and *STAG2*-knockout (KO) cells. Rep1 and Rep2 correspond to different mutant clones. Proteins belonging to the DNA damage repair and replication gene set are highlighted in green. Enrichment  $P$  value was determined using a 1-tailed Fisher's exact test ( $P = 0.024$ ). U937 WT-1, WT-2, *STAG2*-KO5, and *STAG2*-KO6 were used in this experiment. (D) Representative images depicting replication structures of single combed DNA molecules labeled with IdU (red) and CldU (green) in WT and *STAG2*-knockout cells. Quantification of replication origin firing (Orig), progressing replication forks (Prog), and stalled replication forks (Stall) in WT and *STAG2*-mutant cells. Data from 3 WT (U937 WT-1, WT-2, WT-3) and 3 *STAG2*-KO (U937 *STAG2*-KO2, *STAG2*-KO3, *STAG2*-KO4) cell lines combined.  $P < 0.05$  (unpaired Student's  $t$  test). Original magnification, 400 $\times$ . (E) Western blotting for  $\gamma$ -H2Ax. U937 WT-1, WT-2, *STAG2* KO-1, *STAG2* KO-2, *STAG2* KO-3, *STAG2* KO-4, *STAG2* KO-5, and *STAG2* KO-6 were used.  $\beta$ -Actin was a loading control. (F) Western blotting for DNA damage checkpoint proteins ATM, phosphorylated ATM (p-ATM), ATR, p-ATR, CHK1, p-CHK1, CHK2, and p-CHK2 in WT and *STAG2*-mutant cells in the presence and absence of mitomycin C (MMC). Vinculin was a loading control.

*Altered cohesin complex composition and interactome in STAG2-mutant cells.* Having demonstrated that *STAG2* mutations lead to genetic dependencies on *STAG1* and DNA damage repair and replication, we hypothesized that these cohesin-dependent vulnerabilities could be associated with mutant-specific protein complex alterations. To examine the effect of *STAG2* loss on the composition of the cohesin complex, we employed immunoprecipitation using an antibody against the core cohesin ring subunit SMC1A followed by quantitative mass spectrometry (IP-MS) (Supplemental Figure 2B). In WT cells, we detected all members of the cohesin complex, including direct binding partners SMC3 and RAD21, as well as indirect binding partners *STAG1*, *STAG2*, and *PDS5B* (Supplemental Figure 2, C and D; and Supplemental Table 2A). In comparison, examination of *STAG2*-mutant clones revealed *STAG1* to be among the most enriched proteins preferentially incorporated into the cohesin complex in cohesin-mutant cells (hereafter referred to as *STAG1*-cohesin complex for simplicity) (Figure 1C and Supplemental Table 2B). We validated this switch to *STAG1*-containing complexes in *STAG2*-mutant cells using immunoprecipitation followed by Western blotting (Supplemental Figure 2E). A switch from *STAG2* to *STAG1*-cohesin complexes was consistent with the dependency of *STAG2*-mutant cells on *STAG1* (Figure 1A). Unexpectedly, we also observed increased incorporation of *STAG1* into cohesin complexes in cells with heterozygous mutation of a non-*STAG1/2* paralog cohesin subunit, *SMC3* (Supplemental Figure 2, F and G; and Supplemental Table 2C). These studies provide evidence that mutation of either *STAG2* or *SMC3* causes a shift to *STAG1*-containing cohesin complexes.

We next examined whether the shift from *STAG2*- to *STAG1*-containing cohesin complexes is associated with additional changes in its interactome that could explain the genetic dependencies that we had observed. We observed a significant increase in the interaction of the *STAG1*-cohesin complex with proteins involved in DNA replication and DNA damage repair (e.g., *PARP1*, *RPA1-3*;  $P = 0.024$ ) (Figure 1C), transcription factors, and splicing proteins (Supplemental Table 2B). Similarly, we observed changes in the interaction of the *STAG1*-cohesin complex with the DNA damage repair, replication, and splicing machinery in *SMC3*-mutant cells (Supplemental Figure 2F), suggesting that mutations affecting different cohesin subunits may affect the cohesin complex structure and interactome concordantly. These findings demonstrate a high concordance between the cellular processes highlighted by IP-MS experiments and genetic dependency screens in cohesin-mutant cells, especially as it relates to DNA replication and damage repair.

*Stalled replication forks and accumulation of dsDNA breaks in STAG2-mutant cells.* Having found that *STAG2* mutations were associated with a genetic dependency on components of the DNA replication and damage repair pathways, and altered interaction of these proteins with the cohesin complex, we examined whether cells bearing *STAG2* mutations accumulate DNA damage. Cohesin has been shown to organize chromatin loops at DNA replication factories in order to mediate replication stress tolerance and restart stalled replication forks (28–32). Since aberrant replication forks could serve as a potential source of DNA damage in cohesin-mutant cells, we investigated DNA replication fork processivity using a DNA fiber assay (33). Loss of *STAG2* was associated with an increase in the number of stalled replication forks (6% in WT cells versus 25% in *STAG2*-mutant cells,  $P < 0.05$ ) and a tendency to lose replication origin firing (Figure 1D). Furthermore, we observed significant replication fork asymmetry and a 27% decrease in the replication fork rate in *STAG2*-mutant cells (Supplemental Figure 3, A and B), both of which are consistent with replication fork slowing and stalling. Therefore, *STAG2* mutations are associated with abnormal replication fork processivity and stalling, a phenomenon that may be due to aberrant spatial arrangement of replication origins and/or ineffective restarting of replication forks in the absence of a normal cohesin complex.

Stalled replication forks can lead to DNA damage, including dsDNA breaks, if inappropriately resolved. The cohesin complex has been previously implicated in dsDNA break repair and intra-S and G2M checkpoint (34). *STAG1*- versus *STAG2*-containing cohesin complexes have been shown to affect repair pathway



choice, with STAG2-cohesin complex being preferentially involved in sister chromatid homologous recombination repair (35). We therefore examined  $\gamma$ -H2Ax accumulation using immunoblotting as an indicator of dsDNA breaks. We observed accumulation of  $\gamma$ -H2Ax staining under homeostatic conditions across all *STAG2*-mutant cell lines (Figure 1E). This was associated with activation of the ataxia telangiectasia mutated (ATM) and ataxia telangiectasia mutated and Rad3 related (ATR) DNA damage checkpoints as assessed by phosphorylation of ATM and ATR proteins (Figure 1F), even in the absence of mitomycin C treatment, which is predicted to induce DNA damage by blocking both replication and transcription. These data therefore indicate that one of the functional consequences of STAG1-cohesin complexes is aberrant DNA damage repair and increased genomic instability.

*STAG2-mutant cells are sensitive to PARP inhibition in vitro and in vivo.* We next addressed whether altered DNA damage response in *STAG2*-mutant cells creates a vulnerability that can be exploited therapeutically. In our CRISPR screen for genetic dependencies, we found *STAG2*-mutant cells to have a genetic dependency on *PARP1* (Figure 1A,  $P = 0.006$ ), and in our IP-MS experiments, we found an increased association of PARP1 with the cohesin complex in *STAG2*-mutant cells (Figure 1C,  $\log_2FC = 1.03$ ). Furthermore, genetic screens in *Saccharomyces cerevisiae* and *Caenorhabditis elegans* previously identified synthetic lethality interactions between replication fork mediators, including PARP genes, and mutant cohesin (36). We therefore tested sensitivity of *STAG2*-mutant cells to PARP inhibition. PARP inhibitors, including talazoparib, inhibit PARP catalytic activity and trap PARP at the sites of DNA damage, rendering cells that are dependent on nonhomologous end joining repair of dsDNA breaks particularly sensitive to these agents. Treatment with talazoparib resulted in approximately 70-fold increased sensitivity of *STAG2*-mutant cells as compared with WT cells (Figure 2A). In addition, *STAG2*-mutant cells were outcompeted by WT cells in the presence of talazoparib (Figure 2B). We also sought to determine whether mutations in other components of the cohesin complex result in a similar dependency on PARP inhibition. We found that heterozygous inactivation of *SMC3* or *RAD21* was associated with increased sensitivity to PARP inhibition to a similar extent as *STAG2* mutations in U937 and K562 cells (Figure 2C and Supplemental Figure 3C), suggesting that all core cohesin complex mutations we have tested may act as biomarkers of response to PARP inhibition.

We reproduced this effect in xenograft animals injected with individual or competitive mixtures of WT and *STAG2*-mutant AML cells and observed a genotype-specific effect of talazoparib on *STAG2*-mutant cells (Figure 2, D and E). Finally, in order to examine whether response to PARP inhibition in primary human leukemia cells is *STAG2* mutation dependent, we treated *STAG2*-mutant and WT primary AML patient samples with talazoparib and noted a dose- and genotype-dependent sensitivity to the drug (Supplemental Figure 3D). Cumulatively, these studies indicate that cohesin complex mutations result in increased association of DNA repair factors with mutant STAG1-containing cohesin complexes, impaired DNA damage repair, and increased sensitivity to PARP inhibitors.

*Development of cohesin-mutant mouse models of MDS and AML.* In order to extend our observations made in AML cell lines to primary models of *STAG2*-mutant myeloid disease, we developed a syngeneic mouse model in which *Stag2* mutations arise as secondary lesions in the background of clonal hematopoiesis driven by tet methylcytosine dioxygenase 2 (*Tet2*) mutations, as is seen in the development of human MDS (4) (Figure 3A). HSPCs (Lineage-Sc1<sup>+</sup>c-Kit<sup>+</sup> cells) harvested from Mx1-Cre *Cas9* heterozygous C57BL/6 mice were transduced with sgRNA targeting *Tet2* or nontargeting sgRNA (NTG) and transplanted into lethally irradiated SJL recipient mice. Engraftment and clonal expansion of *Tet2*-mutant cells were confirmed by fluorescent protein reporter expression and next-generation sequencing (37) and were not associated with an overt phenotype (Figure 3B). Next, c-Kit-enriched bone marrow cells from mice with *Tet2* mutations (*Tet2* indel fraction 0.62) were transduced with sgRNAs targeting *Stag2* or NTG and transplanted into secondary recipient mice. Cells with *Tet2/Stag2* genetic editing expanded relative to *Tet2/NTG* cells by 2 months posttransplantation (Figure 3C). In contrast to *Tet2*-only mutant mice, *Tet2/Stag2*-mutant mice developed leukocytosis, absolute monocytosis, anemia, and thrombocytopenia (Figure 3D).

Morphologic evaluation of *Tet2/Stag2* bone marrow revealed fewer megakaryocytes and increased hemophagocytosis consistent with macrophage activation in comparison with *Tet2*-only mutant mice (Figure 3E). Next-generation sequencing (NGS) confirmed predicted LOF frameshift mutations in *Tet2* and *Stag2* (mean *Tet2* indel fraction 0.80 in *Tet2/NTG* mice; mean *Tet2* and *Stag2* indel fractions 0.64 and 0.63, respectively, in *Tet2/Stag2* mice). In concordance with our AML cell line data, *Tet2/Stag2*-mutant bone marrow cells exhibited higher levels of dsDNA breaks and increased sensitivity to treatment with talazoparib when

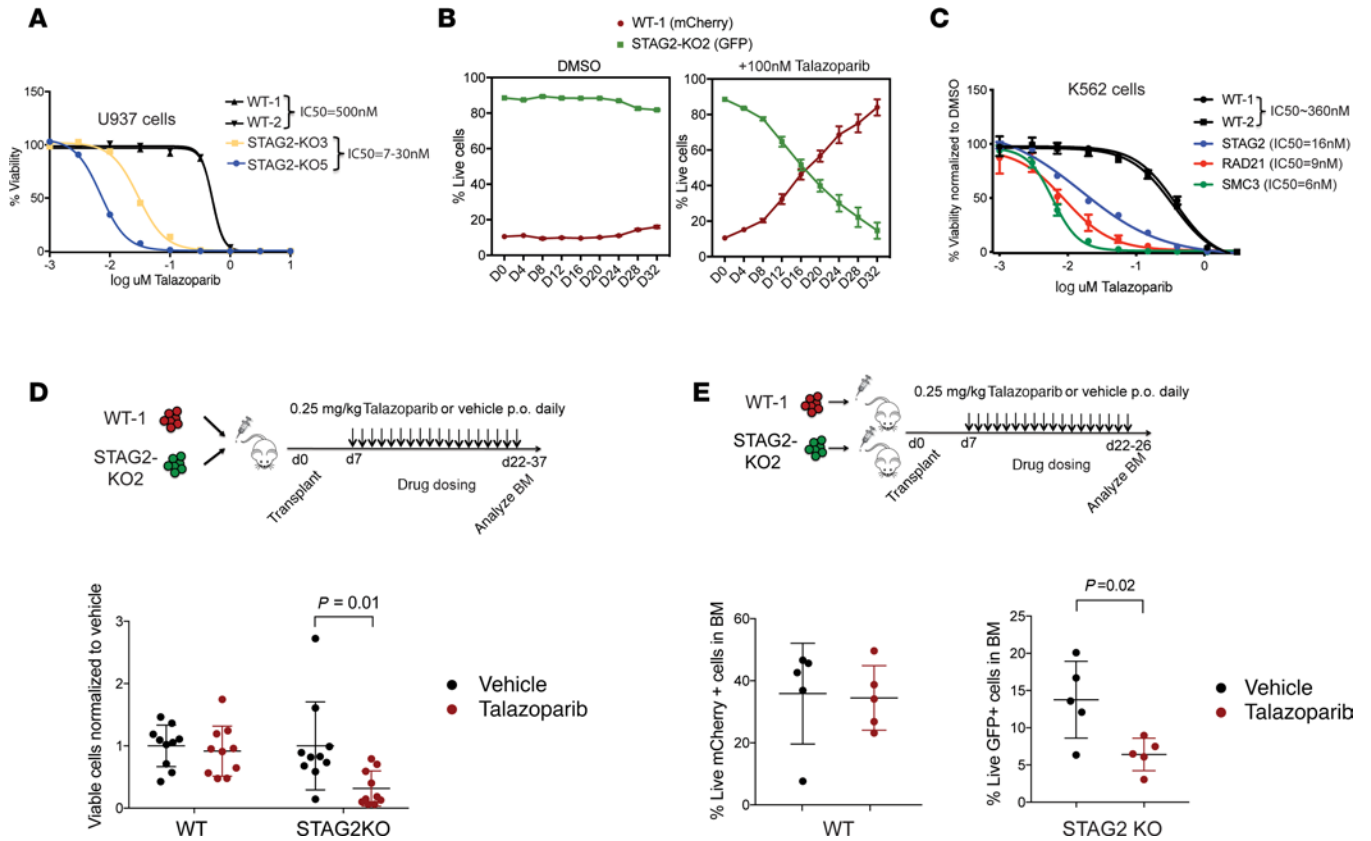


**Figure 2. *STAG2*-mutant AML cell lines are more sensitive to PARP inhibition in vitro and in vivo.** (A) Drug dose response curves of WT and *STAG2*-mutant U937 cell lines treated with the PARP inhibitor talazoparib. U937 WT-1, WT-2, *STAG2* KO-3, and *STAG2* KO-5 cells were used for this experiment.  $IC_{50}$  was calculated on day 12 of treatment. Error bars represent SD of measurements of triplicate technical replicates. (B) Competition assay with WT (U937 WT-1-mCherry) and *STAG2*-knockout (U937 *STAG2*-KO2-GFP) cells mixed in 1:10 ratio in the presence of DMSO or talazoparib (100 nM) in vitro. Error bars represent SD of measurements of triplicate technical replicates. (C) Drug dose response curves of WT and *STAG2*-, *SMC3*-, and *RAD21*-mutant K562 clones treated with talazoparib.  $IC_{50}$  was calculated on day 12 of treatment. Error bars represent SD of measurements of 3 technical replicates. (D) Schematic of the in vivo drug treatment of WT and *STAG2*KO xenografts. WT (U937 WT-1-mCherry) and *STAG2*-knockout (U937 *STAG2*-KO2-GFP) cells were mixed 1:1 and transplanted into NOD/SCID IL-2R $\gamma$  null Tg(IL3, CSF2, KITL) (NSGS) recipients and dosed with talazoparib or vehicle by oral gavage at 0.25 mg/kg once a day. Percentage of live GFP<sup>+</sup> or mCherry<sup>+</sup> cells in the bone marrow was determined using flow cytometry. Mean  $\pm$  SD is shown.  $P = 0.01$  (Student's *t* test).  $n = 10$  mice per group. (E) Schematic of the in vivo drug treatment of WT and *STAG2*-knockout xenografts. WT (U937 WT-1 mCherry) or *STAG2*-knockout (U937 *STAG2*-KO2-GFP) cells were transplanted into NSGS recipients and dosed with talazoparib or vehicle by oral gavage at 0.25 mg/kg once a day. Percentage of live GFP<sup>+</sup> or mCherry<sup>+</sup> cells was determined using flow cytometry. Mean  $\pm$  SD is shown.  $P = 0.02$  (Student's *t* test).  $n = 5$  mice per group.

cultured in vitro (Supplemental Figure 3, E–G). Ex vivo low-dose irradiation of bone marrow cells led to an increase in dsDNA breaks in *Tet2*/NTG cells treated with vehicle but did not appreciably increase already elevated levels of dsDNA breaks in *Tet2*/*Stag2* or any of the talazoparib-treated cells. These studies demonstrate that our CRISPR/Cas9 model with sequential acquisition of *Tet2* and *Stag2* mutations results in aberrant hematopoiesis with *Stag2*-mutant-specific alterations in DNA damage response.

*Talazoparib depletes cohesin-mutant clones in in vivo models of MDS and AML.* *Tet2*/*Stag2* and *Tet2*-mutant clones and the associated hematologic phenotypes were serially transplantable, enabling evaluation of genotype-specific response to the PARP1 inhibitor talazoparib in vivo. Forty recipient mice transplanted with *Tet2* or *Tet2*/*Stag2* mutant bone marrow cells were stratified into treatment groups with talazoparib or vehicle (Figure 4A). Expression of congenic markers and fluorescent reporters linked to *Tet2* and *Stag2* sgRNA expression were used to monitor mice during 4 weeks of treatment. *Tet2*/*Stag2*-mutant mice but not *Tet2*-only mutant mice treated with talazoparib demonstrated a significant loss of mutant cells as determined by NGS and flow cytometry (Figure 4B and Supplemental Figure 4A). In addition, we observed normalization of leukocytosis, monocytosis, and thrombocytopenia in *Tet2*/*Stag2*-mutant mice treated with talazoparib (Figure 4C), which was associated with increased numbers of megakaryocytes on blinded review (Figure 4D and Supplemental Figure 4B,  $P = 0.007$ ).

We next wanted to examine whether response to PARP inhibition is cohesin mutation dependent in primary patient-derived leukemia cell xenografts. We developed 2 unique serially transplantable patient-derived

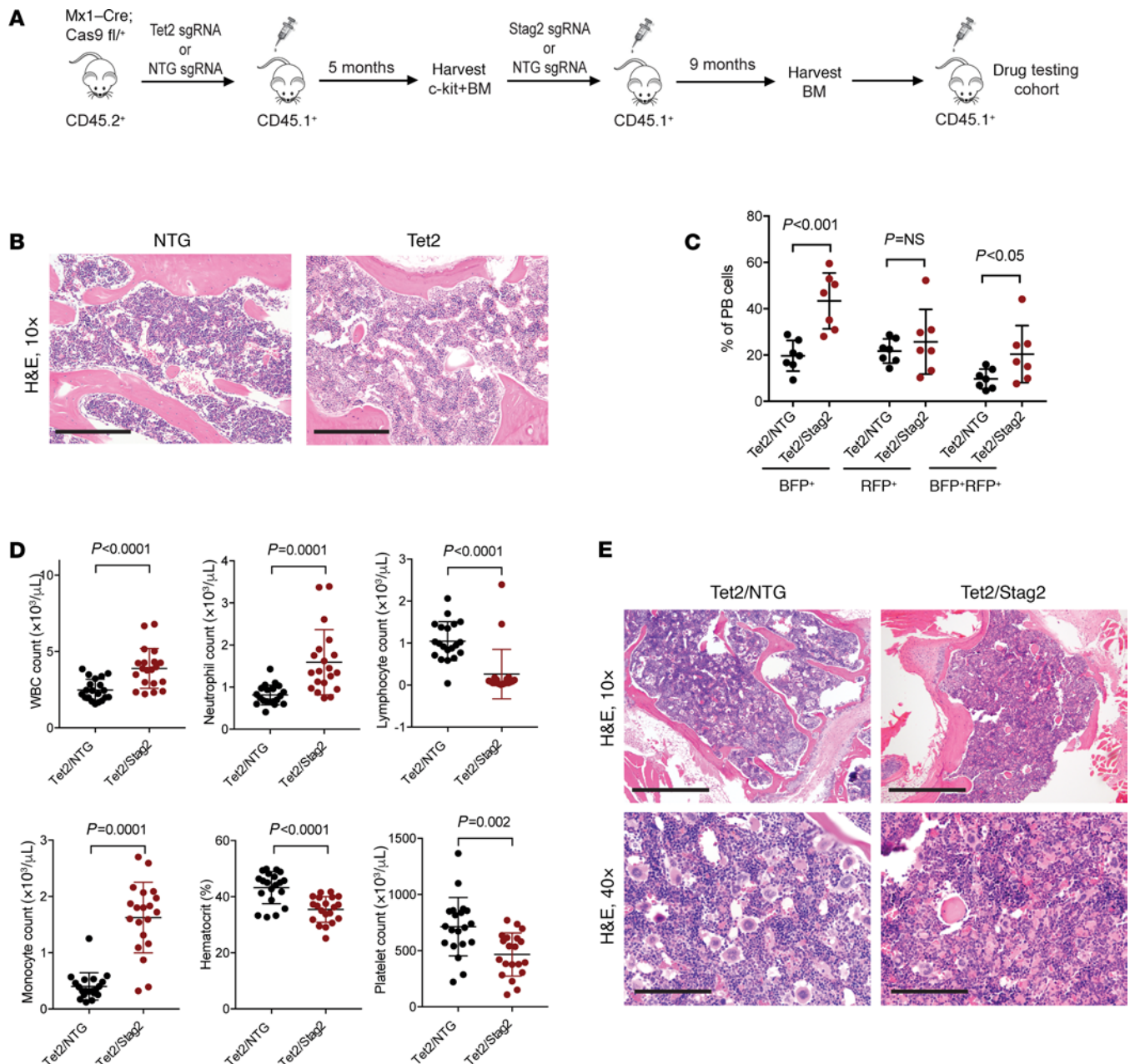


**Figure 3. Development of primary models of cohesin-mutant MDS. (A)** Schematic of the sequential bone marrow transplant used to generate *Tet2/Stag2*-mutant models of myeloid disease. **(B)** Morphologic evaluation of bone marrow section of mice injected with NTG and *Tet2*-mutant cells. H&E staining, 10 $\times$  magnification. No appreciable differences were observed. Scale bar: 0.5 mm. **(C)** Flow cytometry analysis of peripheral blood (PB) samples of mice sequentially transplanted with *Tet2/NTG* and *Tet2/Stag2* 3 months after transplantation. Blue fluorescent protein (BFP) reporter is linked to expression of sgRNA targeting *Stag2*, and red fluorescent protein (RFP) reporter is linked to expression of sgRNA targeting *Tet2*. Expansion of BFP<sup>+</sup> and BFP<sup>+</sup>RFP<sup>+</sup> cells in *Tet2/Stag2* animals.  $n = 7$  per arm. Mean  $\pm$  SD shown. **(D)** Absolute white blood cell (WBC) count, neutrophil count, lymphocyte count, monocyte count, hematocrit, and platelet count were measured in *Tet2/NTG* and *Tet2/Stag2*-mutant mice 12 weeks after bone marrow transplantation. Mean  $\pm$  SD is shown.  $P$  values were determined using the Student's  $t$  test.  $n = 20$  mice per group. **(E)** Morphologic evaluation of bone marrow of a representative *Tet2/NTG* and *Tet2/Stag2*-mutant mouse shows a decrease in megakaryocytes and increased erythrophagocytosis in *Tet2/Stag2*-mutant mice. Images were stained using H&E and imaged at 10 $\times$  (scale bar: 0.5 mm) and 40 $\times$  (scale bar: 0.125 mm) original magnification.

xenograft (PDX) models of *STAG2*- and *RAD21*-mutant AML (Figure 4E and Supplemental Figure 4, C and E) and evaluated the efficacy of talazoparib in both models in vivo. We noted a decrease in disease burden and increased survival of cohesin-mutant PDX models treated with talazoparib as compared with vehicle (Figure 4, F and G; and Supplemental Figure 4, D and F). Therefore, in both primary mouse HSPCs and human AML cells, *STAG2*-mutant cells are selectively sensitive to treatment with talazoparib.



*STAG2 loss alters chromatin compartmentalization and looping.* In order to understand the impact of the aberrant cohesin complex on chromatin compartmentalization and looping, which have been previously linked to DNA replication stress and damage (38), we performed the chromosome conformation analysis Hi-C (39, 40) in a set of *STAG2*-WT and -knockout AML cell lines. This unbiased genome-wide chromosome conformation analysis enables evaluation of chromatin organization at multiple tiers of genome organization, including compartments, TADs, and loops. Compartments are apparent by the plaid pattern of interaction in Hi-C interaction maps (Figure 5A). Analysis of this pattern is routinely performed by principal component analysis, where principal component 1 (PC1) typically captures the positions of compartment domains. The strength of compartmentalization can then be visualized and quantified by rearranging chromatin interaction maps by ordering loci according to their PC1 value to produce compartmentalization “saddle plots” (41). We observed a global weakening of compartmentalization and spatial segregation of active and inactive chromatin domains in *STAG2*-knockout cells (Figure 5B), consistent with more intermixing between expression-rich “A compartments” and expression-poor “B compartments” as defined previously (39). Also, the number and location of TAD boundaries, determined by insulation score analysis (42), was largely preserved between *STAG2*-WT and -mutant cells (Supplemental Figure 5A), but the strength of TAD boundary insulation was globally weakened (Figure 5, C and D; and Supplemental Figure 5B).

Finally, we assessed the effects of *STAG2* loss on the strength and size distribution of positioned loops that are apparent as dots in Hi-C interaction maps and correspond to enriched CTCF-CTCF (CCCTC binding factor–CCCTC binding factor) interactions at the bases of the loops (43). Visual inspection of the heatmaps revealed stronger dots farther away from the diagonal (arrows in Figure 5E). Genome-wide average loop size and loop density can be estimated by analysis of the relationship between interaction frequency ( $P$ ) and genomic distance ( $s$ ) (Supplemental Figure 5C). Specifically, the position of a local maximum in the derivative of  $P(s)$  has been previously shown to represent the average loop size (44). In *STAG2*-WT cells loops were on average 100–200 kb, while in *STAG2*-knockout cells the average loop size was 200–300 kb. In addition, we noted the loop density to be reduced in *STAG2*-knockout cells (Figure 5F).

Combined, these findings show that in the absence of *STAG2*, *STAG1*-containing cohesin complexes extrude larger and somewhat fewer loops. Possibly, *STAG1*-containing cohesin complexes are blocked less efficiently at CTCF sites (resulting in reduced insulation at CTCF sites and TAD boundaries), allowing the loops to more frequently pass CTCF sites and the formation of larger loops. This longer range extrusion process is also expected to lead to more intermixing of A and B compartments.

*STAG2 loss leads to increased colocalization of cohesin with DNA replication and damage repair proteins.* A unifying hypothesis for genetic and pharmacologic dependencies on DNA replication and damage response is that altered chromatin insulation and compartment structure in cohesin-mutant cells leads to shifts in the physical colocalization of proteins involved in these cellular processes. We addressed this hypothesis using super-resolution microscopy. Staining for SMC1A protein, we identified WT and mutant cohesin protein complex aggregates as distinct nuclear puncta (Figure 5G). We observed increased colocalization of the *STAG1*-cohesin complex with PARP1 and RPA1 (Figure 5G). Therefore, we observed *STAG2* mutant-dependent alterations in the physical colocalization of the cohesin complex with DNA damage, concordant with our previously identified changes in the cohesin interactome and genetic dependencies. Put in context with our Hi-C analysis, we hypothesize that these changes may be driven by increased processivity of the *STAG1*-cohesin complex associated with a loss of TAD boundary insulation and longer loop extrusion.

These findings are consistent with a model in which cohesin complexes in WT and cohesin-mutant cells, defined by their unique composition, have differential ability to maintain chromatin organization as it relates to spatial organization of DNA damage repair machinery. Decreased colocalization and function of these components in turn creates vulnerabilities that have the potential to be exploited therapeutically in patients with cohesin-mutated malignancies.

## Discussion

Our studies establish a role for DNA damage, DNA replication, and chromatin architecture in the biology and therapeutic targeting of cohesin-mutant myeloid malignancies. Using genetic screens, IP-MS, chromatin conformation studies, and super-resolution microscopy, we demonstrate that the introduction of cohesin mutations results in a switch from *STAG2* to *STAG1*-cohesin complexes and differential cohesin dependence on DNA damage repair and replication. We observed global spatial chromatin reorganization, including longer loop extrusion, loss of insulation at TAD boundaries, and intermixing of compartments,



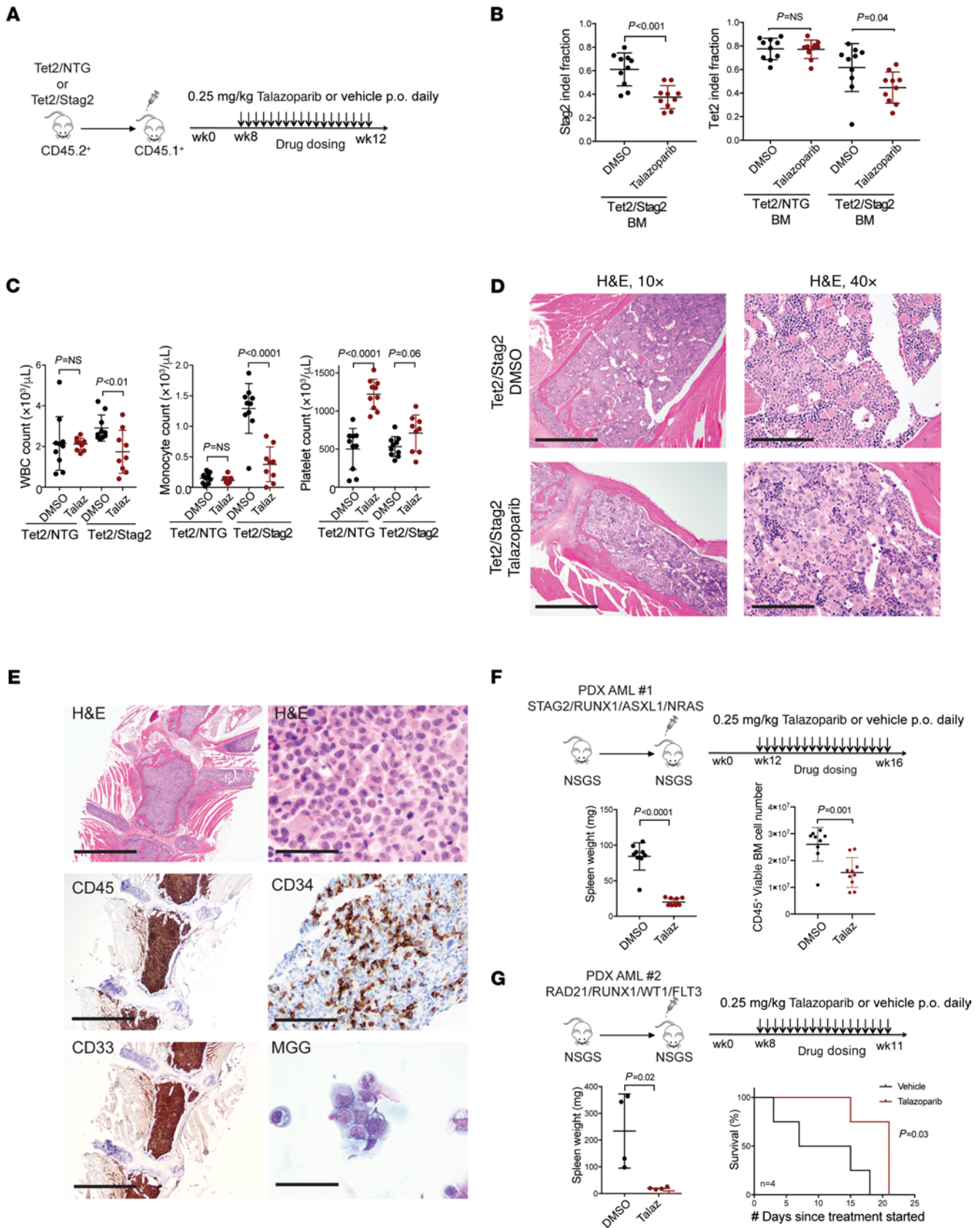


**Figure 4. Talazoparib treatment preferentially depletes cohesin-mutant clones in primary mouse and human cell in vivo models of cohesin-mutant myeloid diseases.** (A) Schematic of the in vivo drug treatment of *Tet2/NTG* and *Tet2/Stag2*-mutant mice with talazoparib. (B) Bone marrow analysis of *Stag2* and *Tet2* indel fraction by NGS demonstrates a genotype-specific response to talazoparib treatment in *Tet2/Stag2* but not *Tet2/NTG*-mutant clones. Mean  $\pm$  SD is shown. *P* values were determined using Student's *t* test. *n* = 10 mice/group. (C) Complete blood count analysis shows normalization of the

WBC, monocyte, and platelet counts in talazoparib-treated *Tet2/Stag2* animals. Mean  $\pm$  SD is shown. *P* values were determined using Student's *t* test. *n* = 10 mice/group. (D) Morphologic evaluation of bone marrow of representative *Tet2/Stag2*-mutant mice treated with talazoparib or DMSO shows an increased megakaryocyte number and persistent erythrophagocytosis in *Tet2/Stag2*-mutant mice treated with talazoparib. Images were stained using H&E and imaged at 10 $\times$  (scale bar: 0.5 mm) and 40 $\times$  (scale bar: 0.125 mm) original magnification. (E) Generation of a *STAG2*-mutant AML PDX model in NSGS mice. Staining with H&E, modified Giemsa May-Grünwald (MGG), and immunohistochemistry shows expansion of immature CD45<sup>+</sup>CD34<sup>+</sup>CD33<sup>+</sup> myeloid blasts in the bone marrow. Images were taken using 10 $\times$  (scale bar: 0.5 mm) and 100 $\times$  original magnification (scale bar: 0.05 mm). (F) Schematic of the in vivo drug treatment of *STAG2*-mutant AML PDX model. Mice showed a decrease in spleen size and human CD45<sup>+</sup> bone marrow disease burden in the talazoparib-treated arm. Mean  $\pm$  SD is shown. *P* values were determined using Student's *t* test. *n* = 9–10 mice/group. (G) Schematic of the in vivo drug treatment of *RAD21*-mutant AML PDX model. Treatment with talazoparib led to a decrease in spleen size and improved overall survival. Mean  $\pm$  SD is shown. *P* values were determined using Student's *t* test and Kaplan-Meier survival analysis. *n* = 4 mice/group.

associated with changes in cohesin interaction with DNA replication and damage machinery, which may explain the basis for the genetic dependency we observed. We extended these findings to LOF mutations in other members of the cohesin complex, including *SMC3* and *RAD21*, and identify cohesin mutations as potential biomarkers of response to treatment with PARP inhibitors.

There are currently very limited therapeutic options for patients with MDS, and no therapies have been identified with selective activity in cohesin-mutant disease. We found that cohesin mutations cause a 70-fold increased sensitivity to PARP inhibition and are a potential biomarker of PARP inhibitor sensitivity in cohesin-mutant myeloid malignancies. PARP inhibitors are currently approved by the FDA for treatment of breast and ovarian cancer in the context of germline *BRCA* mutations and have been previously tested in a phase I study of unselected patients with advanced hematologic malignancies (45). The effect of talazoparib monotherapy in cohesin-mutated AML or MDS with excess blasts is under investigation in a pilot proof-of-concept study (ClinicalTrials.gov identifier NCT03974217). *STAG2*-mutant glioblastoma cells have been previously shown to be sensitive to PARP inhibition in vitro (31, 46), and cohesin mutations may be potential biomarkers of PARP sensitivity in bladder cancer and Ewing sarcoma, where these mutations are common. In addition, combination treatment of hypomethylating agents and PARP inhibition should be considered given sensitivity of cohesin-mutant MDS and genetically engineered CD34<sup>+</sup> cells to hypomethylating agents (9, 47), as well as increased sensitivity of PARP inhibition when administered with low-dose hypomethylating agents in preclinical studies (48). Finally, the role of PARP inhibition as a therapeutic strategy may be efficacious in a wider range of myeloid malignancies characterized by DNA damage repair defects, including *IDH1/2*-AML, *FLT3-ITD*-AML, splicing factor mutant AML, and AML1-ETO rearranged AML (49).

A number of studies have previously examined the effects of complete cohesin loss on chromatin organization, both in the context of an inducible loss of the essential cohesin subunit RAD21 in human cells and loss of the cohesin-loading factor Nipbl in mice (50, 51). These studies confirmed the essential function of the cohesin complex in the formation of topologically associated domains, which is independent of compartment organization. The models used to establish these findings represent a complete loss of cohesin complex, which is not tolerated in human cells and as a result is not implicated in human disease. Patients with cohesin-mutant myeloid malignancies never present with complete, biallelic inactivation of any cohesin subunit, with the notable exception of *STAG2*, which has a paralog, *STAG1*. Complete loss of *STAG1* and *STAG2* was synthetically lethal in our studies as well as in other recent reports (24, 25) and demonstrated in primary mouse HSPCs using *Stag2*-conditional knockout mice (15). The models used in our study aimed to recapitulate the extent of cohesin dysfunction that would be observed in human disease, using both engineered cell lines as well as primary mouse models of cohesin-mutant MDS and AML. Cohesin mutations are early but usually not initiating lesions in myeloid malignancies. Our in vivo model of cohesin-mutant MDS arising in a setting of *Tet2*-mutant clones recapitulates the sequential acquisition of cohesin mutations in the context of *Tet2*-mutant clonal hematopoiesis and the phenotype observed in patients. The approach we developed is highly adaptable and can be used to not only model different stages of disease progression in hematopoietic malignancies but also address the question of order of mutation acquisition and questions of necessity versus sufficiency for transformation using different genetic combinations.

Cohesin has been previously shown to organize chromatin loops at DNA replication factories into rosette-like structures, which allows for organized firing of multiple origins of replication and is disrupted with lower levels of cohesin leading to longer loop formation, similar to our observations with *STAG2*- versus *STAG1*-cohesin complexes (38). How exactly changes in chromatin organization mediated by the switch from *STAG2*- to *STAG1*-containing cohesin complexes in cohesin-mutant cancer cells lead to DNA replication stress and DNA damage repair defects in cells remain to be elucidated.



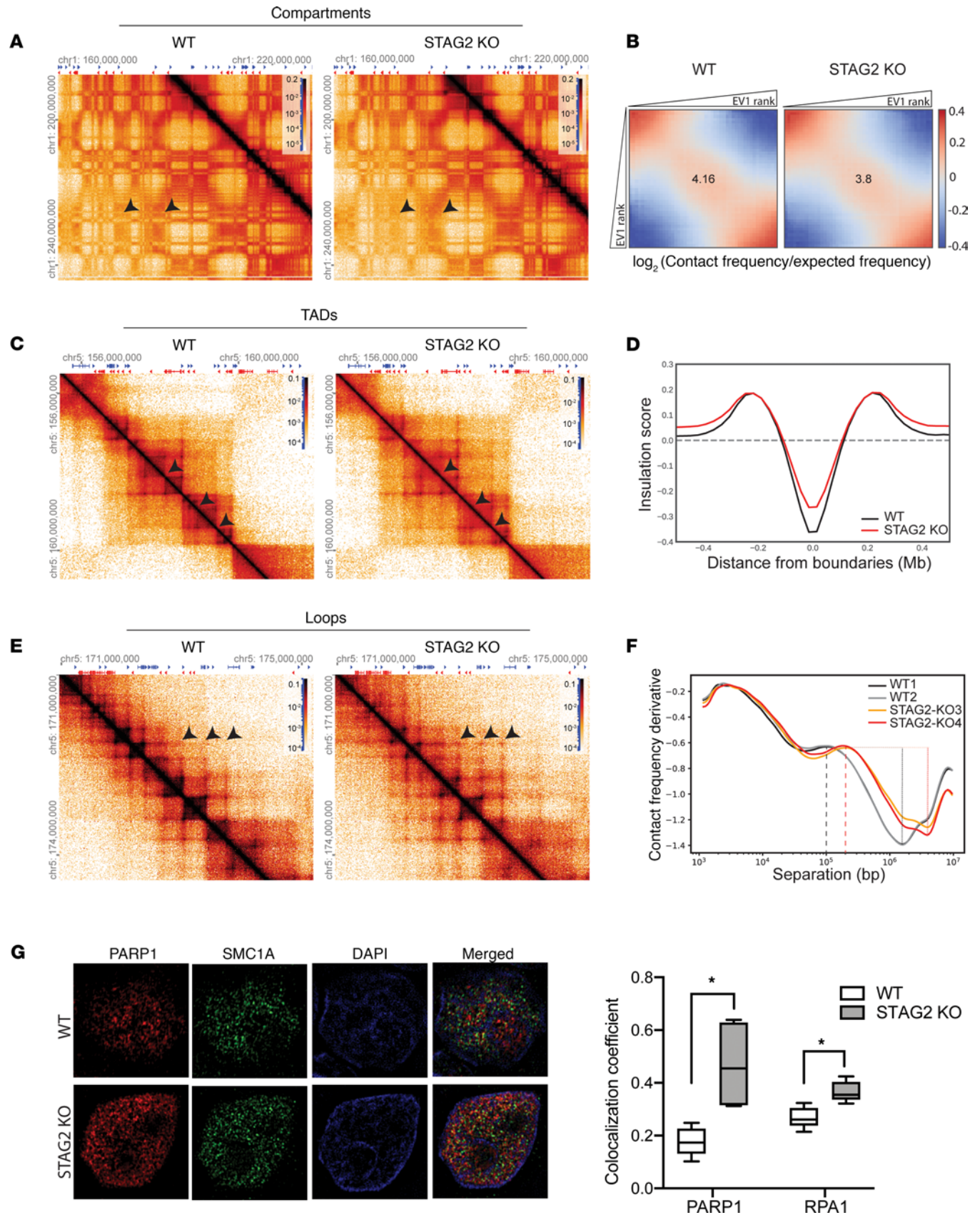


**Figure 5. STAG2 loss disrupts normal chromatin folding and association with DNA replication and damage repair proteins.** (A) Hi-C interaction maps for chromosome 1 binned at 100 kb in WT vs. *STAG2*-knockout cells to visualize compartments. Arrowheads depict examples of weakened compartments. (B) Saddle plots of Hi-C data binned at 100 kb resolution normalized by genomic distance. The saddle plot demonstrates global weakening of compartments in *STAG2*-knockout cells. Heatmaps were generated using Hi-glass from pooled reads from 2 independent WT (U937 WT-1, WT-2) and *STAG2*-knockout (U937 *STAG2*-KO3, *STAG2*-KO4) cell lines. EV1, first eigenvector. (C) Hi-C interaction maps for a genomic region in chromosome 5 binned at 25 kb in WT vs. *STAG2*-knockout cells to visualize TADs. Heatmaps were generated using Hi-glass from pooled reads from 2 independent WT (U937 WT-1, WT-2) and *STAG2*-knockout (U937 *STAG2*-KO3, *STAG2*-KO4) cell lines. Arrowheads depict examples of loss of TAD insulation. (D) Insulation score ( $\lambda_2$ ) as a function of distance from TAD boundaries demonstrates global weakening of insulation at TAD boundaries. (E) Hi-C interaction maps for a genomic region in chromosome 5 binned at 10 kb in WT vs. *STAG2*-knockout cells to visualize loops. Arrowheads depict examples of gain of longer loops. (F) Relationship between interaction frequency ( $P$ ) and genomic distance ( $s$ ) to estimate the average loop size and density demonstrates longer extruded loops in *STAG2*-knockout cells compared with WT cells (represented by dashed lines, U937 WT1, WT2 ~100 kb; U937 *STAG2*-KO3, KO4 ~200 kb) and the density of loops is reduced in *STAG2*-knockout cells (represented by dotted lines). (G) Structured illumination microscopy of SMC1A and PARP1 in WT (U937 WT-1, WT-2) and *STAG2*-knockout (U937 *STAG2*-KO-3, *STAG2*-KO5) cells. Fluorescence signal displayed alone and merged with the nuclear Hoechst stain. Quantification of colocalization of SMC1A with PARP1 or RPA1 was determined using Manders colocalization coefficient. Original magnification, 100 $\times$ . Box and whiskers represent mean  $\pm$  Tukey's. \* $P < 0.0001$ , unpaired Student's  $t$  test.

Significant progress has been made in the last 2 decades in our understanding of the spatial organization of eukaryotic genomes (reviewed in ref. 52). Acquisition of genetic lesions that affect chromatin architecture are common mechanisms of cellular transformation (53, 54). Our study sheds light on how mutations affecting the cohesin complex alter the biology of mutant MDS and leukemia cells in a manner that creates a specific therapeutic vulnerability to PARP inhibitors.

## Methods

**Cell lines.** U937 and K562 cells were obtained from the Broad Institute Cancer Cell Line Encyclopedia, where they were authenticated by short tandem repeat (original source of U937 and K562 cells was ATCC). Cells were grown in RPMI (Invitrogen, Thermo Fisher Scientific) and supplemented with 10% fetal calf serum (MiliporeSigma) and 100 U/mL penicillin and 100  $\mu$ g/mL streptomycin (Invitrogen, Thermo Fisher Scientific).

**Mice.** Female 8- to 10-week-old NSGS mice (NOD/SCID; IL-2R $\gamma$  null; Tg[IL3, CSF2, KITL]; strain 013062) and female 8- to 10-week-old SJL mice (B6.SJL-Ptprc; strain 002014) were obtained from The Jackson Laboratory. Conditional Cas9-knockin mice (strain 026175) and Mx1-Cre mice (strain 003556), both obtained from The Jackson Laboratory, were bred to generate donors for bone marrow transplantation studies. All mice were housed in a pathogen-free animal facility in microisolator cages, and experiments were conducted according to an IACUC-approved protocol at the Broad Institute.

**Generation of cohesin-mutant single-cell clones.** U937-Cas9- and K562-Cas9-expressing cells were first generated by lentiviral transduction with a lentiviral vector pLX-311Cas9 (Addgene 96924). sgRNAs targeting *STAG2*, *SMC3*, and *RAD21* or NTGs were cloned into a minimal backbone plasmid (Addgene 41824) and transfected into U937-Cas9 or K562-Cas9 cells using nucleofection (Lonza, Nucleofector II). GFP<sup>+</sup> cells were single cell sorted into 96-well plates and grown up into single-cell clones, which were confirmed by DNA sequencing of the targeted locus, as well as Western blotting. Of note, since *STAG2* is an X-linked gene that undergoes normal X inactivation in females, patients with predicted LOF *STAG2* mutations are predicted to lack normal *STAG2* expression. Therefore, in both cases of U937 cells and K562 cells, which both carry 2 copies of the X chromosome, we screened for presence of homozygous *STAG2* LOF mutations. See Supplemental Methods.

The following sgRNAs targeting human genes were used in this study individually: *STAG2* (exon 4): TCTGGTCCAAACCGAATGAA; *STAG2* (A1): AATGTCTTACTGCTCTACAA; *STAG2* (A2): CTGAATGTCATCCTCCCGT; *STAG1* (G1): GGAATTAGAGGAGCAGGCCG; *SMC3* (gRNA 1): GATAAAATGAGACGAGCCC; *SMC3* (gRNA 5): GAATATACCATTTACAATC; *RAD21* (gRNA 2): TGTGTTTCGAGTGTAATTTAG; non-targeting (GC1): GACGGAGGCTAAGCGTCGCAA; non-targeting (GC3): GATCGTTTCCGCTTAACGGCG.

The single cell-derived cell lines generated and used in the paper are listed in Supplemental Table 3.

**CRISPR lentiviral transduction.** sgRNAs targeting *STAG2* or *SMC3* were cloned into lentiCRISPRv2 (Addgene 52961).

**Genome-wide CRISPR screening and differential dependency analysis.** A total of 5 *STAG2*-mutant and 6 *STAG2*-WT U937 cells expressing Cas9 were infected with the genome-wide human Avana LentiGuide-Puro CRISPR library (Broad Genetic Perturbations Platform), which contains approximately 75,000 sgRNAs targeting approximately 19,000 genes and 1000 controls, in 2 separate experiments, as previously described



(23). See Supplemental Methods. Raw and processed data have been deposited at figshare: [https://figshare.com/articles/dataset/CRISPR\\_screen\\_of\\_isogenic\\_STAG2\\_mutant\\_cell\\_lines/7120796](https://figshare.com/articles/dataset/CRISPR_screen_of_isogenic_STAG2_mutant_cell_lines/7120796).

*Western blotting, immunoprecipitation, and mass spectrometry.* Details of Western blotting, immunoprecipitation, and IP-MS performed using iTRAQ and TMT6 labeling are detailed in the Supplemental Methods. See complete unedited blots in the supplemental material. The original mass spectra may be downloaded from Mass Spectrometry Interactive Virtual Environment (<http://massive.ucsd.edu>) using the identifier MSV000082970.

*In vitro talazoparib treatment and competition assays.* Talazoparib was purchased from Selleck Chemicals (S7048) and dissolved in DMSO. All drug dose response assays were conducted using CellTiter-Glo luminescent cell viability assay (Promega). Competition experiments were carried out with GFP- and mCherry-labeled cohesin-mutant cells mixed at different ratios and monitored by flow cytometry. See Supplemental Methods.

*DNA fiber assay, cohesion defect analysis, and super-resolution microscopy.* See Supplemental Methods.

*Bone marrow transplantation assays.* C-kit-enriched cells isolated from male donors were transduced with the lentiviral constructs containing *Tet2*, *Stag2*, or nontargeting sgRNA. We specifically used male donors for our experiments since *Stag2* is an X-linked gene and we were interested in modeling loss of *Stag2* expression similar to what has been observed in patients with *STAG2* LOF mutations. Cells were spininfected with lentivirus at 37°C for 90 minutes at 2000 rpm, washed twice, and injected into animals within 6 hours after transduction.

The following sgRNAs targeting mouse genes were used in the study: *Tet2* sgRNA: TCAGGGGC-GATGATGTACAT; *Stag2* sgRNA: TAACACACAAAGACAGTACG.

Please see Supplemental Methods for additional details of transplantation assays and mouse analysis.

*Generation of PDX models.* PDX#1 AML model was generated from bone marrow mononuclear cells of a patient with *STAG2*-mutant AML, confirmed by Dana-Farber Cancer Institute's Rapid Heme Panel sequencing (*STAG2* p.31012\* VAF 0.92; *ASXL1* p.G642fs\* VAF 0.513; *NRAS* p.G13D VAF 0.426; *RUNX1* p.320\* VAF 0.48). PDX#2 AML was generated from a skin lesion of a patient with *RAD21*-mutant AML (*RAD21* p.R586\* VAF 0.287; *FLT3* p.D835Y VAF 0.514; *RUNX1* p.Q265 VAF = 0.295; *WT1* p.R301fs16\* VAF 0.287; *WT1* p.T377fs\* VAF 0.278). See Supplemental Methods.

*In vivo drug treatment.* Two donor *Tet2/Stag2* and 2 donor *Tet2/NTG* mice were used to generate a cohort of mice for in vivo talazoparib experiments. Ten mice per arm were dosed with 0.25 mg/kg talazoparib or vehicle in 0.5% methylcellulose once daily by oral gavage. For drug treatment of PDX models, the mice were dosed with 0.25 mg/kg talazoparib or vehicle in 0.5% methylcellulose ( $n = 9-10$  mice/arm for *STAG2*-mutant PDX,  $n = 4$  mice/arm for *RAD21*-mutant PDX). See Supplemental Methods.

*Indel sequencing analysis.* All sequencing analyses were performed on DNA extracted from 1 million murine bone marrow cells using the QIAamp DNA Micro Kit (Qiagen 56304). A sequential PCR was used to amplify the predicted Cas9 cut sites at both the *Tet2* and *Stag2* loci, as previously described, and all primers are listed below (47). NGS using the MiSeq desktop sequencer (Illumina) was performed, and 300 bp single-end reads were used to identify indels. The depth of sequencing was above 10,000 reads for each gene. CRISPR-Seq, a publicly available method on Terra (<https://terra.bio/>), a cloud-based genomic analysis platform, was used to detect indels. The pipeline has been previously described (47). Reads were mapped against mouse genome build Mm10.

The following sequencing primers were used. For m*Tet2* sgRNA (TCAGGGGCGATGATGTACAT): *FORWARD* 5'- Sequencing Primer - Genomic Primer - 3' ACACTCTTCCCTACACGACGCTCTTC-CGATCT GGTACCCTCAATAGAGAAGACA *REVERSE* 5'- Sequencing Primer - Genomic Primer - 3' GTGACTGGAGTTCAGACGTGTGCTCTTCCGATCT TGGCAGCTCTCCTATCCTT. For m*Stag2* sgRNA(TAACACACAAAGACAGTACG): *FORWARD* 5'- Sequencing Primer - Genomic Primer - 3' ACACTCTTCCCTACACGACGCTCTTCCGATCTTTGGCTGCATAATAATAGCCTAAAC *REVERSE* 5'- Sequencing Primer - Genomic Primer - 3' GTGACTGGAGTTCAGACGTGTGCTCTTC-CGATCT AGTTGATGACTGCTTTGGTAAATG.

*Hi-C methods and data processing.* Hi-C was performed as described previously (40) with some minor modifications. Please see Supplemental Methods for details. The data have been deposited in NCBI's Gene Expression Omnibus (and are accessible through GEO Series accession number GSE165038).

*Statistics.* A *P* value less than 0.05 or an adjusted *P* value/FDR of less than 0.05 was considered significant. Statistical significance of differences in cohesion defects between WT and single and double cohesin knockout cells was determined using a 1-way ANOVA (Figure 1B). Statistical significance of enrichment

of DNA damage repair and replication proteins was determined using a 1-tailed Fisher's exact test (Figure 1C). Statistical significance of differences in replication fork stalling between WT and single and double cohesin knockout cells was determined using a 2-tailed unpaired Student's *t* test (Figure 1D). Statistical significance of differences in leukemia burden between mice treated with talazoparib versus vehicle was determined using a 2-tailed unpaired Student's *t* test (Figure 2, D and E; and Figure 4, F and G). Statistical significance of differences in blood counts of Tet2/NTG and Tet2/Stag2 mice in the presence and absence of treatment with talazoparib was determined using 2-tailed unpaired Student's *t* tests (Figure 3D and Figure 4C). Statistical significance of differences in *Stag2* and *Tet2* indel fraction in the bone marrow of Tet2/NTG and Tet2/Stag2 mice treated with talazoparib or vehicle was determined using 2-tailed unpaired Student's *t* tests (Figure 4B). Statistical significance of differences in survival of *RAD21*-mutant PDX model treated with talazoparib or vehicle was determined using Kaplan-Meier survival analysis (Figure 4G). Statistical significance of differences in colocalizing coefficients of cohesin with PARP or RPA1 protein in *STAG2* WT and mutant cells was determined using 2-tailed unpaired Student's *t* tests (Figure 5G).

*Study approval.* All mouse experiments were conducted according to an IACUC-approved protocol at the Broad Institute.

### Author contributions

ZT and BLE designed the research; ZT, EC, KL, MS, ADD, SAC, JD, and BLE supervised the research; ZT, ALV, RAG, MV, JMKB, AH, CCL, EM, CH, JEH, MD, KDP, SK, and JR performed the research; ZT, ALV, JMKB, AH, CCL, EM, CH, MD, KDP, JR, EC, SVV, MS, and EAM analyzed the data. ZT and BLE wrote the manuscript.

### Acknowledgments

We thank A. Spektor and A. Dall'Agnesse for assistance with confocal microscopy; G. Cowley, S. Younger, and S. Pantel for technical advice; Y. Lee and L. Ali for technical assistance; N. Abdenur for helpful discussions; and D. Neuberg for help with statistical analysis. This work was supported by the NIH (R01HL082945 and 479 P30CA006516), the Edward P. Evans Foundation, the Gabrielle's Angel Foundation, the Leukemia & Lymphoma Society Scholar Award to BLE; the National Human Genome Research Institute (HG003143 to JD); the NIH (5K12CA087723-12 and 1K08HL140138-01), the Leukemia & Lymphoma Society Special Fellow Award (3363-13), the American Society of Clinical Oncology Young Investigator Award, the American Society of Hematology Scholar Award, and the American Society of Hematology/European Hematology Association Translational Research in Hematology Award to ZT; and the NIH (T32GM007753) to SK. BLE and JD are investigators of the Howard Hughes Medical Institute. This work was supported in part by grants from the NIH/National Cancer Institute (NIH/NCI) (55) Clinical Proteomic Tumor Analysis Consortium grants NIH/NCI U24-CA210986 and NIH/NCI U01 CA214125 to SAC. We thank Dana-Farber/Harvard Cancer Center in Boston, Massachusetts, for the use of the Specialized Histopathology Core, which provided histology and immunohistochemistry service. Dana-Farber/Harvard Cancer Center is supported in part by an NCI Cancer Center Support Grant NIH 5 P30 CA06516.

Address correspondence to: Benjamin L. Ebert or Zuzana Tothova, Dana-Farber Cancer Institute, 450 Brookline Avenue, Boston, Massachusetts 02215, USA. Email: benjamin\_ebert@dfci.harvard.edu (BLE). Email: zuzana\_tothova@dfci.harvard.edu (ZT).

1. Losada A. Cohesin in cancer: chromosome segregation and beyond. *Nat Rev Cancer*. 2014;14(6):389–393.
2. Lawrence MS, et al. Discovery and saturation analysis of cancer genes across 21 tumour types. *Nature*. 2014;505(7484):495–501.
3. Leiserson MD, et al. Pan-cancer network analysis identifies combinations of rare somatic mutations across pathways and protein complexes. *Nat Genet*. 2015;47(2):106–114.
4. Sperling AS, et al. The genetics of myelodysplastic syndrome: from clonal haematopoiesis to secondary leukaemia. *Nat Rev Cancer*. 2017;17(1):5–19.
5. Papaemmanuil E, et al. Genomic classification and prognosis in acute myeloid leukemia. *N Engl J Med*. 2016;374(23):2209–2221.
6. Cancer Genome Atlas Research Network, et al. Genomic and epigenomic landscapes of adult de novo acute myeloid leukemia. *N Engl J Med*. 2013;368(22):2059–2074.
7. Haferlach T, et al. Landscape of genetic lesions in 944 patients with myelodysplastic syndromes. *Leukemia*. 2014;28(2):241–247.
8. Papaemmanuil E, et al. Clinical and biological implications of driver mutations in myelodysplastic syndromes. *Blood*. 2013;122(22):3616–3627.
9. Thota S, et al. Genetic alterations of the cohesin complex genes in myeloid malignancies. *Blood*. 2014;124(11):1790–1798.

10. Kon A, et al. Recurrent mutations in multiple components of the cohesin complex in myeloid neoplasms. *Nat Genet.* 2013;45(10):1232–1237.
11. Welch JS, et al. The origin and evolution of mutations in acute myeloid leukemia. *Cell.* 2012;150(2):264–278.
12. Viny AD, et al. Dose-dependent role of the cohesin complex in normal and malignant hematopoiesis. *J Exp Med.* 2015;212(11):1819–1832.
13. Mazumdar C, et al. Leukemia-associated cohesin mutants dominantly enforce stem cell programs and impair human hematopoietic progenitor differentiation. *Cell Stem Cell.* 2015;17(6):675–688.
14. Mullenders J, et al. Cohesin loss alters adult hematopoietic stem cell homeostasis, leading to myeloproliferative neoplasms. *J Exp Med.* 2015;212(11):1833–1850.
15. Viny AD, et al. Cohesin members Stag1 and Stag2 display distinct roles in chromatin accessibility and topological control of HSC self-renewal and differentiation. *Cell Stem Cell.* 2019;25(5):682–696.
16. Holzmann J, et al. Lesson from the stoichiometry determination of the cohesin complex: a short protease mediated elution increases the recovery from cross-linked antibody-conjugated beads. *J Proteome Res.* 2011;10(2):780–789.
17. Lindsley RC, et al. Acute myeloid leukemia ontogeny is defined by distinct somatic mutations. *Blood.* 2015;125(9):1367–1376.
18. Walker CJ, et al. No evidence for microsatellite instability in acute myeloid leukemia. *Leukemia.* 2017;31(6):1474–1476.
19. Kojic A, et al. Distinct roles of cohesin-SA1 and cohesin-SA2 in 3D chromosome organization. *Nat Struct Mol Biol.* 2018;25(6):496–504.
20. Wutz G, et al. ESCO1 and CTCF enable formation of long chromatin loops by protecting cohesin(STAG1) from WAPL. *Elife.* 2020;9:52091.
21. Casa V, et al. Redundant and specific roles of cohesin STAG subunits in chromatin looping and transcriptional control. *Genome Res.* 2020;30(4):515–527.
22. Ochi Y, et al. Combined cohesin-RUNX1 deficiency synergistically perturbs chromatin looping and causes myelodysplastic syndromes. *Cancer Discov.* 2020;10(6):836–853.
23. Doench JG, et al. Optimized sgRNA design to maximize activity and minimize off-target effects of CRISPR-Cas9. *Nat Biotechnol.* 2016;34(2):184–191.
24. Benedetti L, et al. Synthetic lethal interaction between the tumour suppressor STAG2 and its paralog STAG1. *Oncotarget.* 2017;8(23):37619–37632.
25. van der Lelij P, et al. Synthetic lethality between the cohesin subunits STAG1 and STAG2 in diverse cancer contexts. *Elife.* 2017;6:26980.
26. Eisfeld AK, et al. The mutational oncoprint of recurrent cytogenetic abnormalities in adult patients with de novo acute myeloid leukemia. *Leukemia.* 2017;31(10):2211–2218.
27. Heidinger-Pauli JM, et al. Systematic reduction of cohesin differentially affects chromosome segregation, condensation, and DNA repair. *Curr Biol.* 2010;20(10):957–963.
28. Terret ME, et al. Cohesin acetylation speeds the replication fork. *Nature.* 2009;462(7270):231–234.
29. Tittel-Elmer M, et al. Cohesin association to replication sites depends on rad50 and promotes fork restart. *Mol Cell.* 2012;48(1):98–108.
30. Wu N, Yu H. The SMC complexes in DNA damage response. *Cell Biosci.* 2012;2:5.
31. Mondal G, et al. A requirement for STAG2 in replication fork progression creates a targetable synthetic lethality in cohesin-mutant cancers. *Nat Commun.* 2019;10(1):1686.
32. Benedict B, et al. WAPL-dependent repair of damaged DNA replication forks underlies oncogene-induced loss of sister chromatid cohesion. *Dev Cell.* 2020;52(6):683–698.
33. Nieminuszczy J, et al. The DNA fibre technique — tracking helicases at work. *Methods.* 2016;108:92–98.
34. Watrin E, Peters JM. The cohesin complex is required for the DNA damage-induced G2/M checkpoint in mammalian cells. *EMBO J.* 2009;28(17):2625–2635.
35. Kong X, et al. Distinct functions of human cohesin-SA1 and cohesin-SA2 in double-strand break repair. *Mol Cell Biol.* 2014;34(4):685–698.
36. McLellan JL, et al. Synthetic lethality of cohesins with PARPs and replication fork mediators. *PLoS Genet.* 2012;8(3):1002574.
37. Song WJ, et al. Haploinsufficiency of CBFA2 causes familial thrombocytopenia with propensity to develop acute myelogenous leukaemia. *Nat Genet.* 1999;23(2):166–175.
38. Guillou E, et al. Cohesin organizes chromatin loops at DNA replication factories. *Genes Dev.* 2010;24(24):2812–2822.
39. Lieberman-Aiden E, et al. Comprehensive mapping of long-range interactions reveals folding principles of the human genome. *Science.* 2009;326(5950):289–293.
40. Belaghzal H, et al. Hi-C 2.0: an optimized Hi-C procedure for high-resolution genome-wide mapping of chromosome conformation. *Methods.* 2017;123:56–65.
41. Nora EP, et al. Targeted degradation of CTCF decouples local insulation of chromosome domains from genomic compartmentalization. *Cell.* 2017;169(5):930–944.
42. Crane E, et al. Condensin-driven remodelling of X chromosome topology during dosage compensation. *Nature.* 2015;523(7559):240–244.
43. Rao SS, et al. A 3D map of the human genome at kilobase resolution reveals principles of chromatin looping. *Cell.* 2014;159(7):1665–1680.
44. Gassler J, et al. A mechanism of cohesin-dependent loop extrusion organizes zygotic genome architecture. *EMBO J.* 2017;36(24):3600–3618.
45. Mufti GJ, et al. Results of a phase 1 study of BMN 673, a potent and specific PARP-1/2 inhibitor, in patients with advanced hematological malignancies. *Haematologica.* 2014;99(suppl 1):33–34.
46. Bailey ML, et al. Glioblastoma cells containing mutations in the cohesin component STAG2 are sensitive to PARP inhibition. *Mol Cancer Ther.* 2014;13(3):724–732.
47. Tothova Z, et al. Multiplex CRISPR/Cas9-based genome editing in human hematopoietic stem cells models clonal hematopoiesis and myeloid neoplasia. *Cell Stem Cell.* 2017;21(4):547–555.
48. Muvarak NE, et al. Enhancing the cytotoxic effects of PARP inhibitors with DNA demethylating agents — a potential therapy for cancer. *Cancer Cell.* 2016;30(4):637–650.
49. Fritz C, et al. PARP goes the weasel! Emerging role of PARP inhibitors in acute leukemias [published online May 7, 2020]. *Blood Rev.* <https://doi.org/10.1016/j.blre.2020.100696>.

50. Rao SSP, et al. Cohesin loss eliminates all loop domains. *Cell*. 2017;171(2):305–320.
51. Schwarzer W. Two independent modes of chromatin organization revealed by cohesin removal. *Nature*. 2017;551(7678):51–56.
52. Dekker J, Mirny L. The 3D genome as moderator of chromosomal communication. *Cell*. 2016;164(6):1110–1121.
53. Hnisz D, et al. Activation of proto-oncogenes by disruption of chromosome neighborhoods. *Science*. 2016;351(6280):1454–1458.
54. Flavahan WA, et al. Insulator dysfunction and oncogene activation in IDH mutant gliomas. *Nature*. 2016;529(7584):110–114.
55. Zhang X, et al. Identification of focally amplified lineage-specific super-enhancers in human epithelial cancers. *Nat Genet*. 2016;48(2):176–182.